Journal of Molecular Liquids xxx (xxxx) xxx

Contents lists available at ScienceDirect

Journal of Molecular Liquids

journal homepage: www.elsevier.com/locate/molliq

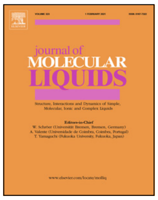

Enhanced photocatalytic degradation of dimethyl phthalate by magnetic dual Z-scheme iron oxide/mpg-C_3N_4/BiOBr/polythiophene heterostructure photocatalyst under visible light

Shaoxiu Li *, Chan Lai, Changhui Li, Jintang Zhong, Zhifeng He, Qiuyi Peng, Xi Liu, Bohan Ke

School of Civil and Transportation Engineering, Guangdong University of Technology, No100, Waihuan Xi Guangzhou Higher Education Mega Center, Panyu District, Guangzhou 510006, Guangdong, PR China

ARTICLE INFO

Article history:
Received 25 February 2021
Revised 30 June 2021
Accepted 5 July 2021
Available online xxxx

Keywords:
Photocatalysis
g-C_3N_4
BiOBr
Z-scheme heterostructure
Dimethyl phthalate
Polythiophene

ABSTRACT

A new magnetic dual Z-scheme heterostructure photocatalyst, consisting of mesoporous graphitic carbon nitride (mpg-C_3N_4), BiOBr, polythiophene (PTh), and magnetic iron oxide, was developed, and its structural, optical, and electrochemical properties were analyzed. The photocatalyst was employed for the degradation of dimethyl phthalate (DMP) in water under visible light to evaluate its photocatalytic activity. The results revealed that the photocatalytic activity of the new heterostructure photocatalyst was superior to that of its single-component counterparts. The reaction kinetics of photocatalytic DMP degradation followed pseudo first-order kinetics and the reaction rate constant was 3.7- and 4.5-fold higher than those of pristine g-C_3N_4 and BiOBr, respectively. The enhanced photocatalytic performance was chiefly attributed to the dual Z-scheme heterostructure generated between mpg-C_3N_4, PTh, and BiOBr, which effectively hindered the recombination of photogenerated electron and hole pairs in mpg-C_3N_4 and BiOBr, improving the photogenerated carrier transfer efficiency. Radical trapping test results indicated that the active species, h^+, $\cdot O_2^-$, and $\cdot OH$, coexisted during the photocatalytic reaction process, and that h^+ played a major role in the destruction of DMP molecules. DMP was degraded into intermediate small-molecule products, such as acids and alcohols, which were ultimately mineralized to CO_2 and H_2O. The magnetic property of the new heterostructure photocatalyst enabled its straightforward separation from water using magnetic separation technology for further reuse. This study provides a new material and method for the effective removal of DMP from aqueous solution.

1. Introduction

Dimethyl phthalate (DMP) is a plasticizer widely used in the manufacture of plastic packaging, toys, decorative materials, and various household necessities. It is also an endocrine disruptor with carcinogenic, teratogenic, and mutagenic properties, and is therefore detrimental to human health [1]. DMP has been detected in the atmosphere, water, soil, and even in biological samples. Moreover, it is not readily biodegradable and its removal via conventional water treatment is challenging.

Photocatalytic technology has been shown to be effective for the degradation of organic pollutants [2–6]. In this arena, the conventional TiO_2 photocatalyst is gradually being replaced by new photocatalysts as TiO_2 is active only under ultraviolet light [7–9]. Semiconductor materials, bismuth oxyhalides (BiOX, X = Cl, Br, I), have been extensively investigated as photocatalysts due to several advantages, such as high chemical stability, a suitable band gap, and favorable optical properties [10–14]. Among the bismuth-based semiconductors, bismuth oxybromide (BiOBr) is a typical photocatalyst with a unique layered structure consisting of $[Bi_2O_2]^{2+}$ layers interleaved by halogen ions. The narrow band gap energy (2.54–2.91 eV) and stable photocatalytic activity of BiOBr [15–18] has prompted considerable research into its applicability for the photocatalytic degradation of organic pollutants and hydrogen generation via water splitting under visible light [19–23]. However, the prompt recombination of photogenerated electron-hole pairs reduces its photocatalytic performance. Therefore, numerous approaches for improving charge carrier migration have been developed to date. Among them, the construction of a heterojunction between BiOBr and other materials has been extensively studied [24–29].

In recent years, the non-metallic graphitic carbon nitride (g-C_3N_4) photocatalyst has been investigated as an alternative to the conventional TiO_2 photocatalyst for the degradation of organic pollutants and hydrogen production due to important advantages,

---

* Corresponding author.
E-mail address: water@gdut.edu.cn (S. Li).

https://doi.org/10.1016/j.molliq.2021.116947
0167-7322/

Please cite this article as: S. Li, C. Lai, C. Li et al., Enhanced photocatalytic degradation of dimethyl phthalate by magnetic dual Z-scheme iron oxide/mpg-C_3N_4/BiOBr/polythiophene heterostructure photocatalyst under visible light, Journal of Molecular Liquids, https://doi.org/10.1016/j.molliq.2021.116947

such as responsiveness to visible light, a narrow band gap, favorable thermal stability, and cost-efficient and straightforward preparation [30–34]. However, the photocatalytic activity of pristine g-C_3N_4 is restricted by its small specific surface area (SSA) and low separation efficiency of photogenerated electron-hole pairs. Furthermore, its narrow absorption range in the visible region results in the inadequate utilization of visible light. Thus, a variety of methods, such as surface modification, precious metal doping, and heterojunction construction, have been implemented to improve the photocatalytic activity of g-C_3N_4 [35–40]. Mesoporous graphitic carbon nitride (mpg-C_3N_4) is often prepared via templating and acid etching of g-C_3N_4 to enlarge its SSA [41,42]. The combination of BiOBr and g-C_3N_4 is considered to be a favorable heterojunction as these two materials have a well-matched band, which promotes charge carrier transfer [43–48].

On the other hand, although nanoparticle photocatalysts are efficient and prolific, their separation from water is challenging, limiting their practical application. This drawback can be addressed by magnetizing the nanoparticles. Magnetic nanoparticles can be separated from water using magnetic separation technology, and reused [49–53]. This approach enables the use of nanoparticles for water treatment.

In this study, mpg-C_3N_4 was prepared and subsequently magnetized to generate magnetic mpg-C_3N_4 (M−mpg−C_3N_4), which was used to generate a composite with BiOBr. To expand the absorption range of visible light and further improve the photocatalytic activity, polythiophene (PTh), a conductive polymer exhibiting an excellent capacitance performance, good conductivity, and light absorption over the full wavelength band [54] was doped into the M−mpg−C_3N_4/BiOBr composite. Thus, the M−mpg−C_3N_4/BiOBr/PTh photocatalyst was prepared, and was then used to degrade DMP under visible light. In this study, M−mpg−C_3N_4/BiOBr/PTh was characterized, and its photocatalytic performance for the degradation of DMP was investigated. Additionally, the photocatalytic degradation mechanism was discussed. This study provides an effective material and method for the removal of DMP from water.

2. Experimental section

2.1. Materials

Urea (purity ≥ 99%), tertiary butyl alcohol, and Na_2-EDTA were sourced from Tianjin Fuchen Chemical Reagent Co., Ltd. SiO_2 sol (30% solid) was purchased from LUDOX, USA. NH_4HF_2 and 1, 4-benzoquinone (purity ≥ 97%) were provided by MACKLIN, Shanghai, China. $Bi(NO_3)_3{\cdot}5H_2O$ was sourced from Tianjin Kemiou Chemical Reagent Co., Ltd., KBr was purchased from Tianjin Baishi Chemical Industry Co., Ltd., Dimethyl phthalate (purity ≥ 99.5%) was sourced from the Tianjin Damao Chemical Reagent Factory. Ethanol was obtained from Tianjin Fuyu Chemical Co., Ltd. Polythiophene was purchased from Guangdong Wengjiang Reagent Co., Ltd. $(NH_4)_2Fe(SO_4)_2{\cdot}6H_2O$ was obtained from Tianjin Yongda Chemical Reagent Co., Ltd., and $NH_4Fe(SO_4)_2{\cdot}12H_2O$ from Shanghai Aladdin Reagent Co., Ltd. The reagents used in the study were of analytical grade, except where mentioned above.

2.2. mpg-C_3N_4 preparation

SiO_2 sol was added to urea in a 1:3 mass ratio, followed by the addition of distilled water until dissolution of urea to obtain a mixed SiO_2 and urea solution. The mixed solution was stirred at 90 °C to remove the water and obtain a white solid, which was subsequently ground into powder, placed in a crucible, completely wrapped and sealed with aluminum foil, and heated at 550 °C in a muffle furnace for 4 h at a heating rate of 2.2 °C/min. After cooling to room temperature, a yellow powder was obtained, which was then ground, sieved, and stirred in 4 M NH_4HF_2 at room temperature for 48 h to remove SiO_2. Next, the treated powder was washed with distilled water followed by ethanol and dried at 70 °C overnight to obtain templated g-C_3N_4.

A certain amount of templated g-C_3N_4 was stirred for 30 min in 40 ml of 0.5 M nitric acid. Subsequently, the mixture was kept in a reaction kettle at 160℃ for 6 h. After cooling to room temperature, the resulting powder was successively washed with distilled water and ethanol, and dried at 70 °C overnight to afford the acid-etched product, mpg-C_3N_4.

2.3. Magnetization of mpg-C_3N_4

mpg-C_3N_4, $(NH_4)_2Fe(SO_4)_2{\cdot}6H_2O$ and $NH_4Fe(SO_4)_2{\cdot}12H_2O$ were prepared in a 2.5:1 mass ratio of mpg-C_3N_4 to theoretically generated Fe_3O_4, and a 1:1.43 molar ratio of Fe^{2+} to Fe^{3+}. $NH_4Fe(SO_4)_2{\cdot}12H_2O$ was dissolved in 75 ml of distilled water and heated to 60℃ in a constant temperature water bath. Meanwhile, mpg-C_3N_4 was dispersed in 125 ml distilled water via ultrasonic treatment for 15 min, followed by heating and stirring. When the mpg-C_3N_4 suspension reached 60℃, $(NH_4)_2Fe(SO_4)_2{\cdot}6H_2O$ and the heated $NH_4Fe(SO_4)_2{\cdot}12H_2O$ solution were added to the mpg-C_3N_4 suspension. An alkaline solution comprising Na_2CO_3 and NaOH in a molar ratio of 5:3 was slowly dropped into the mpg-C_3N_4 suspension until the pH was above 11.0 and stirring was continued at 60 ℃ for 30 min, followed by aging at the same temperature for 30 min. Finally, the product was washed several times with distilled water to remove the bases, dried at 70 °C for 8 h, and then ground and sieved to afford magnetic mpg-C_3N_4 powder, denoted as M−mpg−C_3N_4.

2.4. Preparation of M−mpg−C_3N_4/BiOBr/PTh composite material

The M−mpg−C_3N_4, $Bi(NO_3)_3{\cdot}5H_2O$, and PTh dispersion was weighed with a 1:5 mass ratio of M−mpg−C_3N_4 to theoretically produced BiOBr, the PTh dispersion accounted for 0.25% of the total weight of M−mpg−C_3N_4/BiOBr/PTh. The ratio of the M−mpg−C_3N_4, $Bi(NO_3)_3{\cdot}5H_2O$, and PTh was determinated by single factor experiments and orthogonal experiment. The $Bi(NO_3)_3{\cdot}5H_2O$ was completely dissolved in 20 ml of ethylene glycol, followed by the addition of the PTh dispersion and stirring for 15 min. M−mpg−C_3N_4 was then added, followed by stirring for 15 min and ultrasonication for another 15 min to obtain solution A. KBr was weighed according to the stoichiometric relationship between $Bi(NO_3)_3{\cdot}5H_2O$ and KBr in the reaction, dissolved in 20 ml of distilled water and slowly dropped into solution A, which was subsequently stirred at 400 r/min for 30 min at room temperature, and then kept in a reaction kettle at 140℃ for 18 h. Finally, the product was washed successively with distilled water and ethanol, and dried at 70 °C overnight to obtain the M−mpg−C_3N_4/BiOBr/PTh composite.

2.5. Characterization

Field emission scanning electron microscopy and transmission electron microscopy (SEM/TEM) measurements were conducted using an SU8220 field emission scanning electron microscope (Hitachi, Japan) and a Talos F200S transmission electron microscope (FEI, Czech Republic), respectively. Energy dispersive X-ray spectroscopy (EDS) was detected using energy dispersive X-ray spectrometry (Oxford X-Max50, UK). X-ray diffraction (XRD) spectroscopy was conducted using a D8 Advance X-ray diffractometer (Bruker, Germany). X-ray photoelectron spectra (XPS) were collected using an Escalab 250Xi X-ray photoelectron spectrometer (Thermo Fisher Scientific, USA). Fourier transform infrared (FTIR)

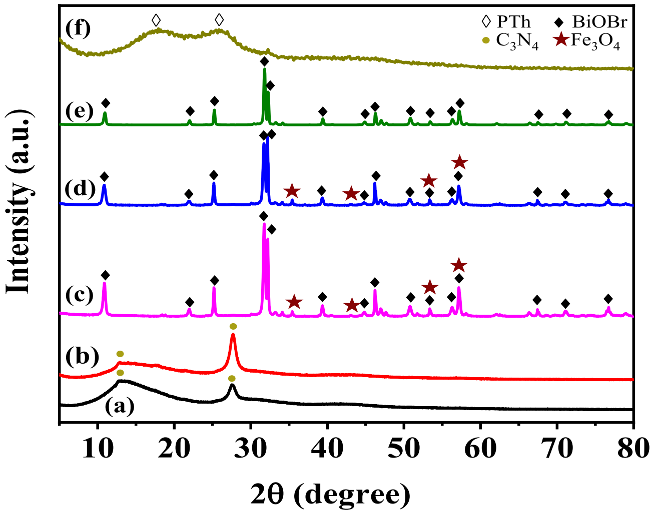

Fig. 1. XRD patterns of (a) g-C_3N_4, (b) mpg-C_3N_4, (c) M−mpg−C_3N_4/BiOBr, (d) M−mpg−C_3N_4/BiOBr/PTh, (e) BiOBr and (f) PTh.

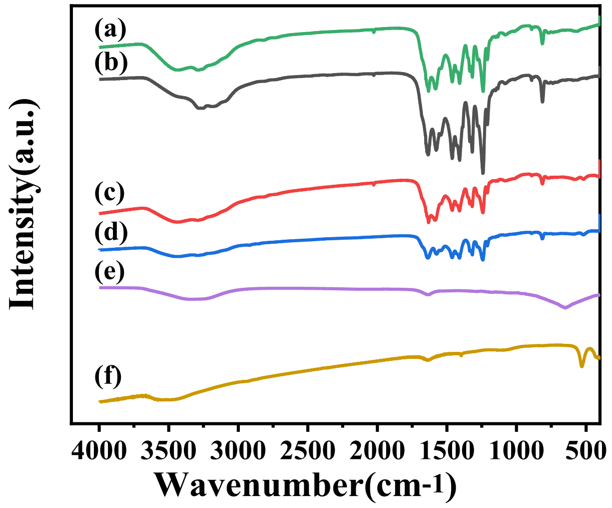

Fig. 2. FTIR spectra of (a) g-C_3N_4, (b) mpg-C_3N_4, (c) M−mpg−C_3N_4/BiOBr, (d) M−mpg−C_3N_4/BiOBr/PTh, (e) PTh and (f) BiOBr.

spectra were recorded on a Nicolet IS50 Fourier transform infrared spectrometer (Thermo Fisher Scientific, USA). The SSA was analyzed using an ASAP 2460 specific surface area and pore analyzer (Micromeritics, USA). Magnetism was measured using a 7404 vibrating-sample magnetometer (VSM) (LakeShore, USA). UV–vis diffuse reflectance spectra (UV–vis DRS) were obtained using an UV-3600 Plus ultraviolet–visible spectrophotometer (Hong Kong, China). Photoluminescence (PL) was measured using a Fluorolog-3 fluorescence spectrophotometer (HORIBA Instruments Incorporated, USA). Electrochemical impedance spectroscopy (EIS) was conducted using a 1470E electrochemical workstation (AMETEK GB, Ltd., UK). The degradation products of DMP were detected using ultra performance liquid chromatography (UPLC) coupled with Q Exactive orbitrap mass spectrometry (Thermo Fisher Scientific, USA).

2.6. Photocatalytic experiments

A certain amount of photocatalyst was added to 50 ml DMP solution of a certain concentration. The mixture was shaken under dark conditions for 30 min. Subsequently, photodegradation was induced under illumination with a 500 W GXZ500 xenon lamp. The solution was collected and filtered at regular intervals, and the filtrate was analyzed using a LC-210 high-performance liquid chromatography (HPLC) instrument (INESA, China).

3. Results and discussion

3.1. Characterization of materials

3.1.1. Microstructure characterization

The XRD patterns of g-C_3N_4 and its modified materials are shown in Fig. 1. In the XRD patterns of g-C_3N_4 and mpg-C_3N_4, two obvious diffraction peaks were observed at 12.94 and 27.63°, which were characteristic diffraction peaks of g-C_3N_4, indicating that the mpg-C_3N_4 remained the component of g-C_3N_4. The XRD patterns shown in Fig. 1c and 1d contained the characteristic peaks of BiOBr at 10.87, 21.96, 25.18, 31.77, 32.16, 39.34, 44.84, 46.21, 50.10, 53.37, 56.30, 57.16, and 67.43°, conforming to the existence of BiOBr in the composites of M−mpg−C_3N_4/BiOBr and M−mpg−C_3N_4/BiOBr/PTh. The diffraction peaks at 2θ = 35.73, 43.06, 53.37, and 57.16° were attributed to Fe_3O_4 and γ-Fe_2O_3 [55], suggesting that the magnetic substances were successfully loaded onto the composites. Nevertheless, the characteristic peaks of mpg-C_3N_4 were barely visible in the XRD pattern of M−mpg−C_3N_4/BiOBr/PTh due to the low amount of mpg-C_3N_4, as was previously reported [43]. Similarly, the characteristic peaks of PTh were absent, which is in agreement with Mahmoudian's findings [56].

The FTIR spectra of g-C_3N_4, mpg-C_3N_4, M−mpg−C_3N_4/BiOBr, and M−mpg−C_3N_4/BiOBr/PTh are presented in Fig. 2. Several characteristic g-C_3N_4 peaks are visible in Fig. 2a; the peak at 813 cm^{-1} was ascribed to the characteristic bending vibration of the triazine ring [57], the peaks at 1240 and 1317 cm^{-1} were attributed to the stretching vibrations of the C—NH—C connecting unit. The peaks at 1410, 1462, and 1632 cm^{-1} were assigned to the C—N heterocyclic skeletal stretching vibrations of the aromatic rings in g-C_3N_4. The FTIR spectrum of mpg-C_3N_4 (Fig. 2b) was identical to that of g-C_3N_4, indicating that the structure of g-C_3N_4 remained unchanged upon SiO_2 templating and acid etching. In the spectrum depicted in Fig. 2c, new bands appeared at approximately 519 and 578 cm^{-1} and were attributed to Bi—O and Fe—O stretching vibrations, respectively, confirming that the composite contained iron oxide and BiOBr. In addition, the characteristic PTh peaks can be seen in Fig. 2e; the peak at 1638 cm^{-1} was attributed to the asymmetric stretching vibration of C = C of thiophene ring [58], the bending vibration peak of the C—S bond in thiophene ring appeared at 651 cm^{-1}. But the C—S characteristic peak was not present in the spectrum of [58]Fig. 2d, which could be ascribed to the low amount of PTh in the composite, the observation was consistent with the literature [58].

Fig. 3 illustrates the SEM and TEM images of g-C_3N_4 and the other photocatalysts, as well as the EDS spectrum of M−mpg−C_3N_4/BiOBr/PTh. As shown in Fig. 3A, pure g-C_3N_4 presented a layered graphite-like structure with interlayer stacking of the conjugated carbocyclic plane. Fig. 3B shows the significantly etched surface of mpg-C_3N_4 particles, which increase the SSA to provide more active reaction sites on the particle surfaces. Fig. 3C revealed the typical layered nanosheet structure of BiOBr dispersed on the surface of mpg-C_3N_4 forming a heterojunction. Furthermore, as seen in Fig. 3D, the degree of BiOBr stacking increased after adding PTh to M−mpg−C_3N_4/BiOBr compared to that in M−mpg−C_3N_4/BiOBr (Fig. 3C) and BiOBr (Fig. 3E). The SEM images indicated that M−mpg−C_3N_4, BiOBr, and PTh were successfully combined using the hydrothermal method to form a heterojunction. The TEM image in Fig. 3G shows the presence of numerous holes shaped

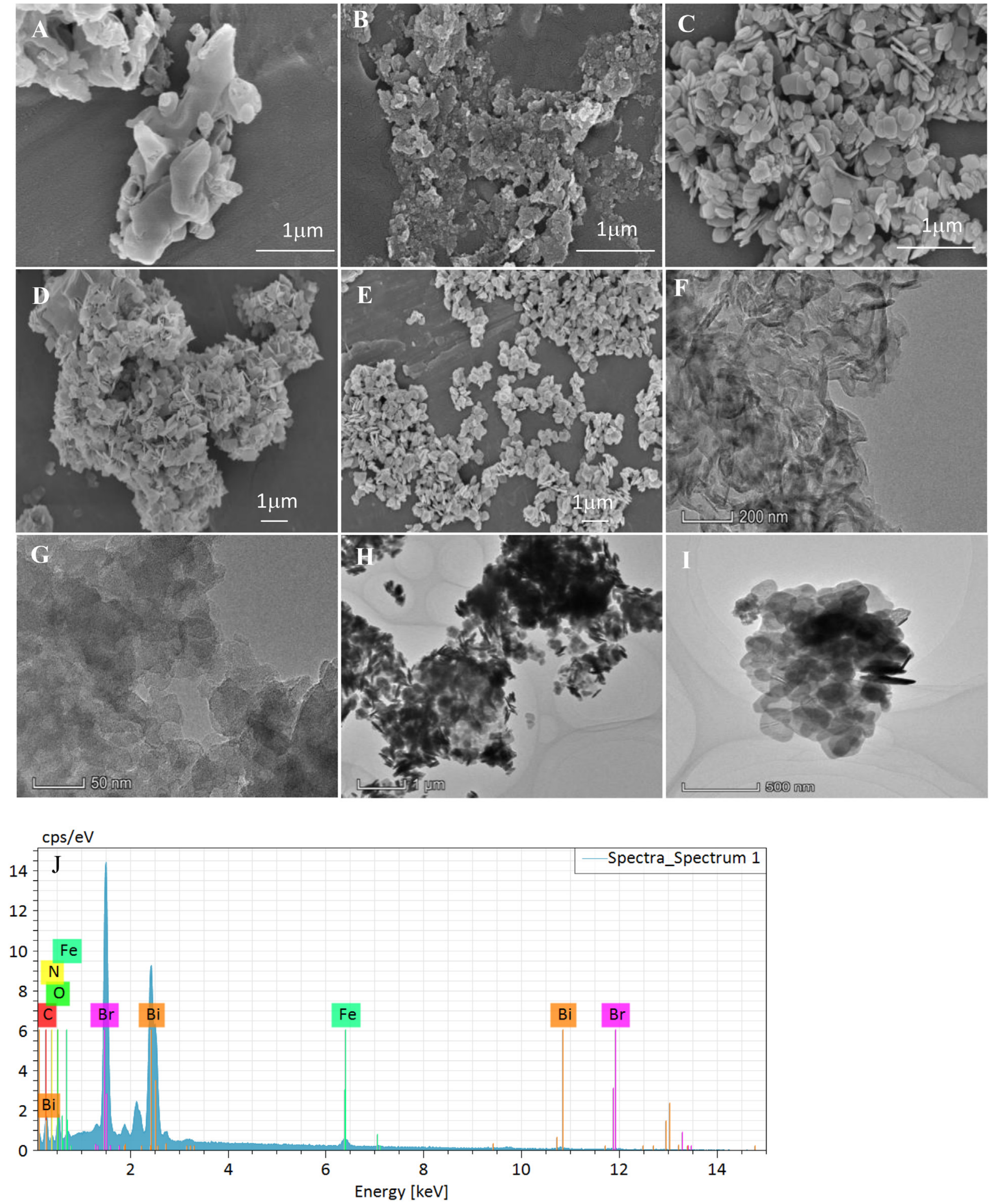

Fig. 3. SEM images of (A) g-C_3N_4, (B) mpg-C_3N_4, (C) M−mpg−C_3N_4/BiOBr, (D) M−mpg−C_3N_4/BiOBr/PTh and (E) BiOBr; TEM images of (F) g-C_3N_4, (G) mpg-C_3N_4, (H) M−mpg−C_3N_4/BiOBr and (I) M−mpg−C_3N_4/BiOBr/PTh; (J) EDS spectrum of M−mpg−C_3N_4/BiOBr/PTh.

according to the SiO_2 template, created upon template removal by NH_4HF_2. BiOBr flakes were deposited and combined with mpg-C_3N_4 to generate the heterojunction evident in Fig. 3H, and the heterojunction of M−mpg−C_3N_4/BiOBr/PTh is depicted in Fig. 3I. EDS spectrum of M−mpg−C_3N_4/BiOBr/PTh in Fig. 3J demonstrated that M−mpg−C_3N_4/BiOBr/PTh contained elements of C, O, N, Bi, Br, and Fe. S is the representative element in PTh composition, however, as PTh was present in a low amount in the M−mpg−C_3N_4/BiOBr/PTh composite, the absence of S can be expected.

The XPS spectra of M−mpg−C_3N_4/BiOBr/PTh are displayed in Fig. 4. It is evident from the M−mpg−C_3N_4/BiOBr/PTh survey spectrum (Fig. 4a) that the composite consisted primarily of C, O, N, Bi, Br, and Fe elements. The C 1 s spectrum shown in Fig. 4b contained three peaks at 284.59, 285.73, and 288.23 eV, which were attributed to C—C in graphitic carbon, sp2- hybridized C, and the N—C = N group [43], respectively, suggesting the existence of g-C_3N_4 in the M−mpg−C_3N_4/BiOBr/PTh composite. The N1s spectrum (Fig. 4c) was deconvoluted into three distinct peaks located at 401.28,

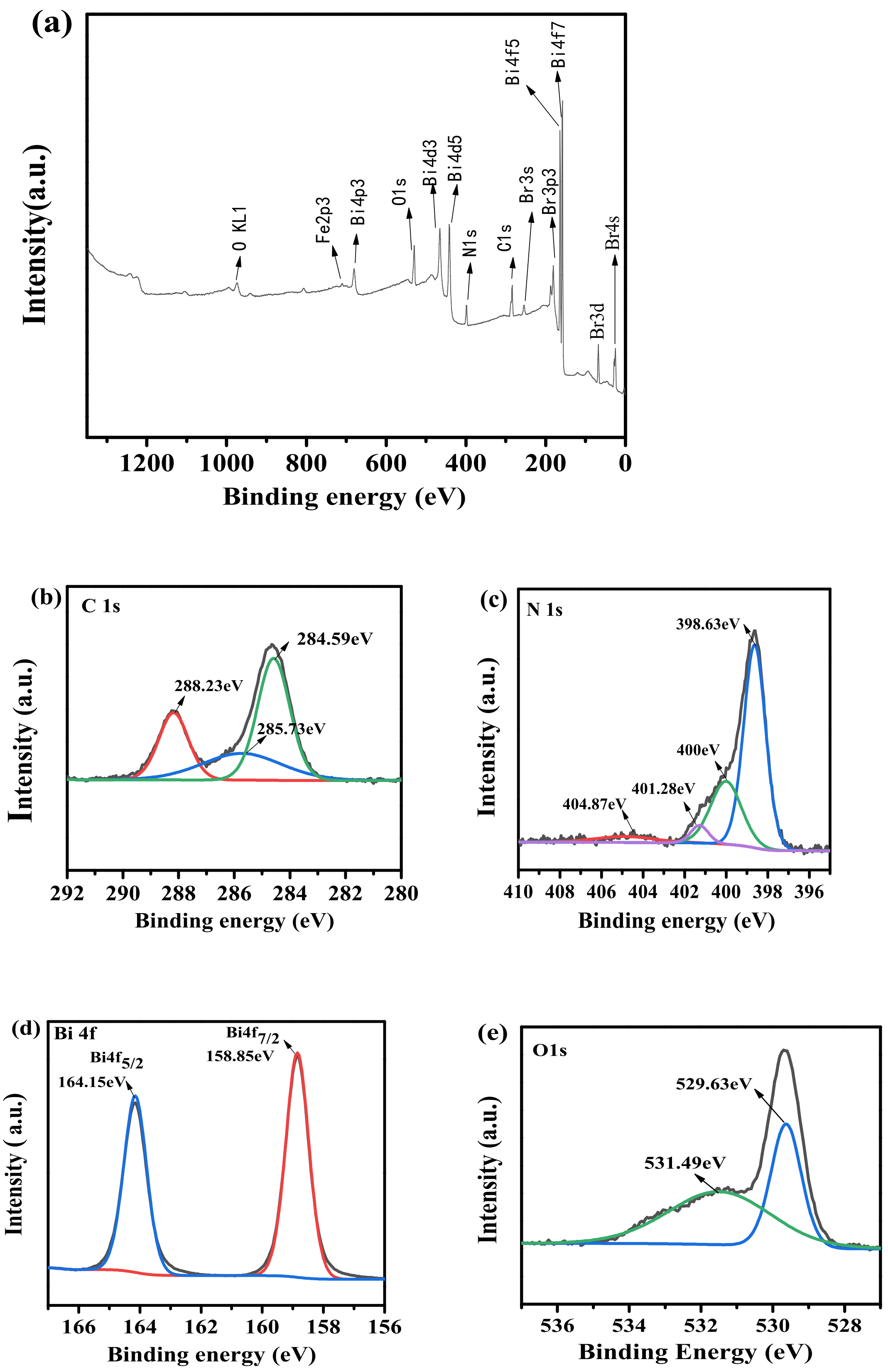

Fig. 4. XPS spectra of M−mpg−C_3N_4/BiOBr/PTh, (a) survey spectrum , (b) C1s, (c) N1s, (d) Bi 4f, (e) O1s, (f) Br3d, (g) Fe2p and (h) S2s.

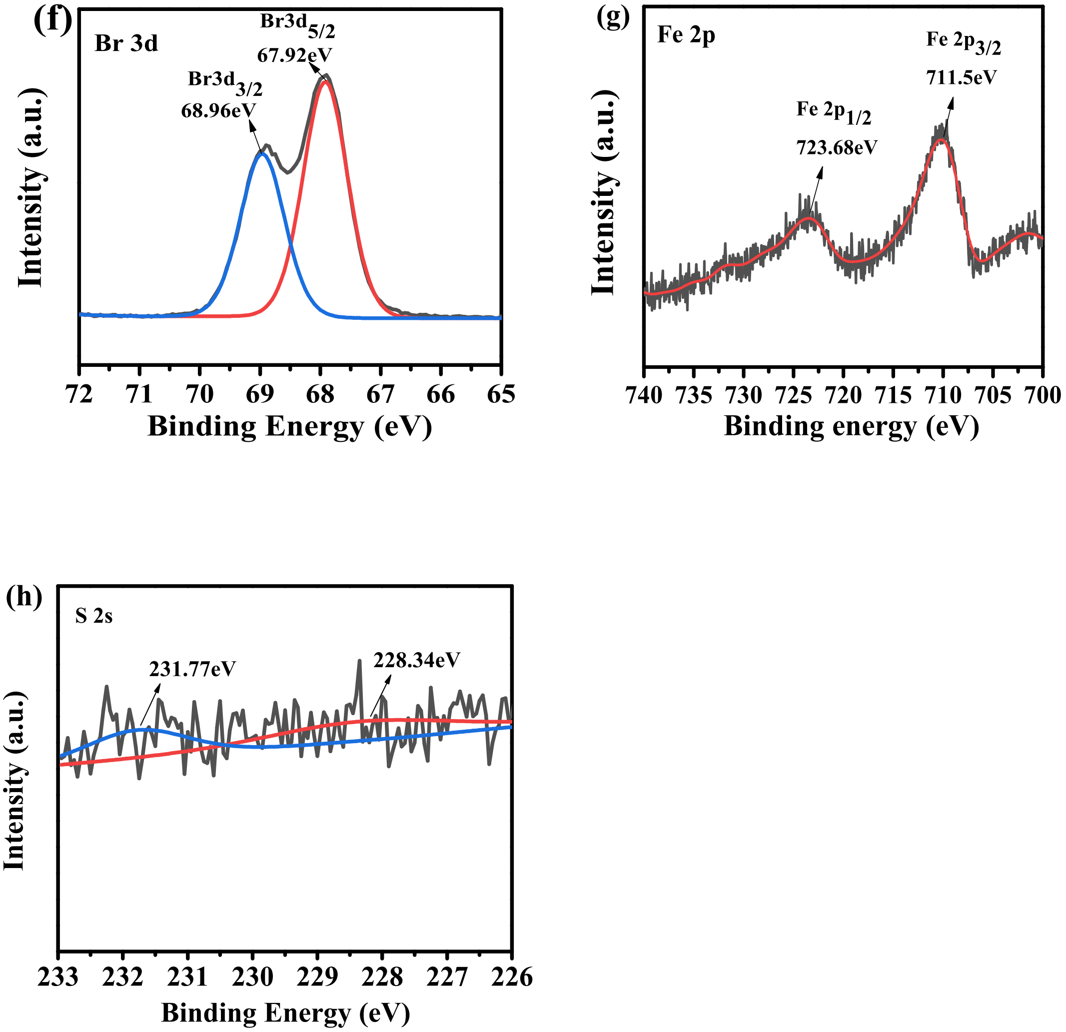

Fig. 4 (*continued*)

400, and 398.63 eV, as well as one weak peak at 404.87 eV; the three distinct peaks were assigned to N—H, N—(C)$_3$ and C—N = C groups, respectively, while the weak peak may have arisen from the electron localization of the heptazine ring [59]. The Bi 4f spectrum (Fig. 4d) displayed peaks at 164.15 and 158.85 eV, ascribed to Bi 4f$_{5/2}$ and Bi 4f$_{7/2}$ of Bi^{3+} of the Bi–O bond, respectively. The XPS spectrum of O 1 s contained two peaks at 529.63 and 531.49 eV (Fig. 3e), assigned to the oxygen atoms in the Bi–O crystal lattice and to those of surface hydroxyl groups [57], respectively. The Br 3d peaks at 67.92 and 68.96 eV (Fig. 3f) corresponded to Br 3d$_{5/2}$ and Br 3d$_{3/2}$, respectively. The Fe 2p spectrum (Fig. 3g) displayed typical peaks at 711.5 and 723.68 eV, ascribed to Fe 2p$_{3/2}$ and Fe 2p$_{1/2}$ of oxidized iron species [60,61], respectively. Two peaks, at 228.34 and 231.77 eV, were observed in the S 2s spectrum, but they were so inconspicuous that they were absent in the survey spectrum. This is in accordance with the XRD, FTIR and EDS analysis results.

Fig. 5 displays the nitrogen adsorption–desorption isotherms and the pore size distribution of the photocatalysts. As shown in Fig. 5A, type H3 hysteresis loops existed in the adsorption–desorption isotherms, it was caused by the flaky and granular particles or particles with slit voids, indicating that the shapes of the photocatalysts was flaky and granular, this was in agreement with the results of SEM and TEM analysis. In addition, it is evident that M−mpg−C_3N_4/BiOBr/PTh is a mesoporous material seen from Fig. 5B. The SSAs of g-C_3N_4, mpg-C_3N_4, and M−mpg−C_3N_4/BiOBr/PTh, were determined to be 57.382, 90.129, and 21.391 m^2/g, respectively. The SSA of g-C_3N_4 increased after SiO_2 templating and acid etching, but decreased after it was combined with iron oxide, BiOBr, and PTh. It is possible that BiOBr covered the surface of mpg-C_3N_4 and iron oxide particles filled the holes of mpg-C_3N_4. Nonetheless, the photocatalytic activity of M−mpg−C_3N_4/BiOBr/PTh was superior to that of mpg-C_3N_4, principally as a result of the curtailed recombination of photogenerated electron-hole pairs and enhanced photogenerated carrier transfer efficiency in the heterojunction of M−mpg−C_3N_4/BiOBr/PTh.

The ferromagnetic hysteresis loops of magnetic g-C_3N_4 and M−mpg−C_3N_4/BiOBr/PTh are presented in Fig. 6. The large curvature of the two hysteresis loops suggests that the two materials can be readily magnetized and are strongly ferromagnetic, which is beneficial for their separation from the aqueous phase and recovery for recycling in practical applications. Moreover, the magnetization curve does not display remanence or coercivity, indicating that magnetic g-C_3N_4 and M−mpg−C_3N_4/BiOBr/PTh are paramagnetic. The saturation magnetization of magnetic g-C_3N_4 and M−mpg−C_3N_4/BiOBr/PTh were 18.70 and 11.31 emu/g, respectively. The finding that the former was higher than the latter was attributed to the lower amount of magnetic iron oxides per unit mass of M−mpg−C_3N_4/BiOBr/PTh composite compared to that in magnetic g-C_3N_4. The magnetic measurement results verified that magnetic iron oxides were incorporated into the M−mpg−C_3N_4/BiOBr/PTh composite.

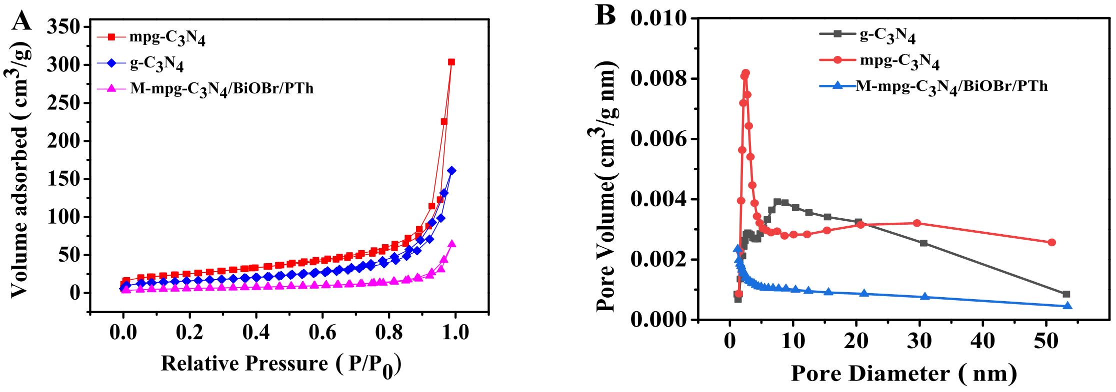

Fig. 5. (A) Nitrogen adsorption–desorption isotherms and (B) the pore size distribution of photocatalysts.

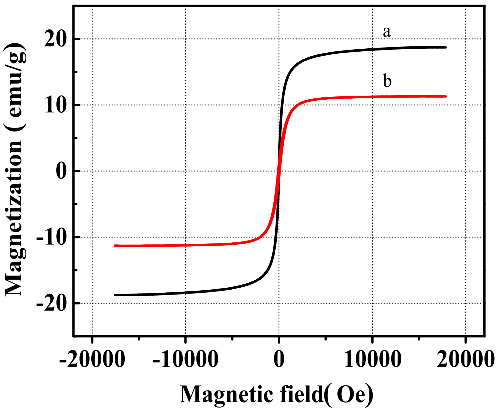

Fig. 6. Ferromagnetic hysteresis loops of (a) magnetic g-C_3N_4 and (b) M–mpg–C_3N_4/BiOBr/PTh.

3.1.2. Optical properties

Fig. 7A illustrates the UV–vis DRS of g-C_3N_4, mpg-C_3N_4, M–mpg–C_3N_4/BiOBr, and M–mpg–C_3N_4/BiOBr/PTh. Absorption edges were observed at 412, 421, 427, and 443 nm for g-C_3N_4, mpg-C_3N_4, M–mpg–C_3N_4/BiOBr, and M–mpg–C_3N_4/BiOBr/PTh, respectively, which indicated that the visible light absorption range broadened with the formation of the composites. According to the UV–Vis DRS and the Kubelka-Munk transformation [62], the plot of $(\alpha h\upsilon)^{1/2}$ vs. photon energy was constructed as shown in Fig. 7B, and the band gap energy of g-C_3N_4, mpg-C_3N_4, M–mpg–C_3N_4/BiOBr, and M–mpg–C_3N_4/BiOBr/PTh were estimated as 2.72, 2.68, 2.55 eV, and 2.46 eV, respectively, indicating that the band gap width in the composites was reduced compared to that of pristine g-C_3N_4, which is beneficial for enhancing the photocatalytic performance.

The fluorescence spectra of g-C_3N_4, mpg-C_3N_4, M–mpg–C_3N_4/BiOBr, and M–mpg–C_3N_4/BiOBr/PTh are depicted in Fig. 8A. Evidently, the PL intensity decreased considerably after M–mpg–C_3N_4 was combined with BiOBr, and decreased slightly after the introduction of PTh, indicating that the heterojunction structure of M–mpg–C_3N_4/BiOBr/PTh improved photogenerated charge separation and inhibited the recombination of photogenerated electron-hole pairs.

EIS analysis was used to illustrate the separation of photogenerated charges in the photocatalysts. The EIS measurement results of g-C_3N_4, mpg-C_3N_4, M–mpg–C_3N_4/BiOBr, and M–mpg–C_3N_4/BiOBr/PTh are shown in Fig. 8B, wherein the order of the photogenerated charge transmission impedance values was determined as g-C_3N_4 > mpg-C_3N_4 > M-mpg-C_3N_4/BiOBr > M-mpg-C_3N_4/BiOBr/PTh. Among them, M–mpg–C_3N_4/BiOBr/PTh presented the smallest arc radius and the lowest charge transfer resistance, suggesting that this composite will have the highest separation efficiency of photogenerated charge carriers and the fastest interface charge transfer of the four photocatalysts. This is consistent with the results of fluorescence spectroscopy measurements.

3.2. Photocatalytic activity

The photocatalytic DMP degradation efficiency of the photocatalysts is illustrated in Fig. 9A. It is evident that the adsorptive DMP removal rate of mpg-C_3N_4 was higher than that of pristine g-C_3N_4 after 30 min without light absorption, as a result of the increase in the SSA of g-C_3N_4 after SiO_2 templating and acid etching. On the other hand, the photocatalytic DMP degradation efficiency of M–mpg–C_3N_4/BiOBr was significantly higher than that of g-C_3N_4,

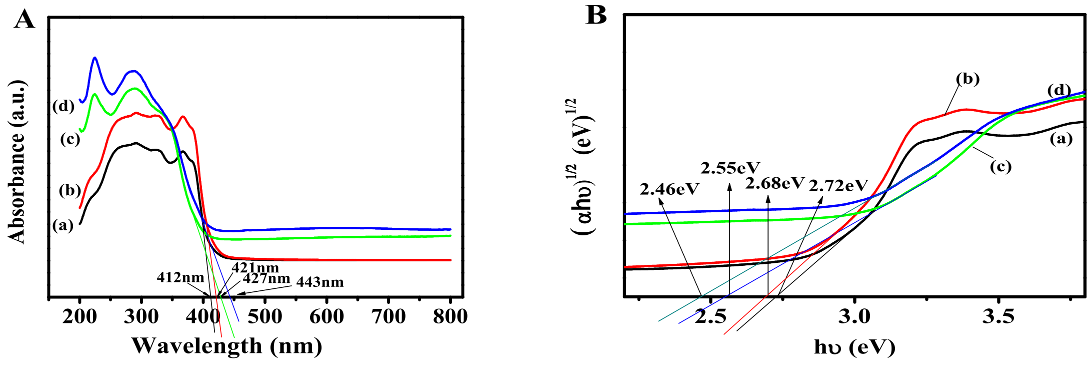

Fig. 7. UV–vis diffuse reflective spectra of (a) g-C_3N_4, (b) mpg-C_3N_4, (c) M–mpg–C_3N_4/BiOBr and (d) M–mpg–C_3N_4/BiOBr/PTh.

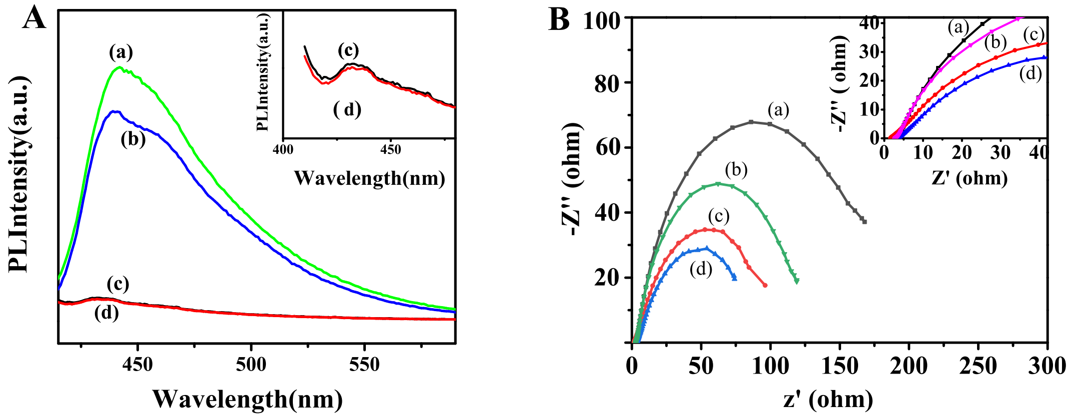

Fig. 8. (A) Photoluminescence spectra and (B) electrochemical impedance spectroscopyof (a) g-C_3N_4, (b) mpg-C_3N_4, (c) M−mpg−C_3N_4/BiOBr and (d) M−mpg−C_3N_4/BiOBr/PTh.

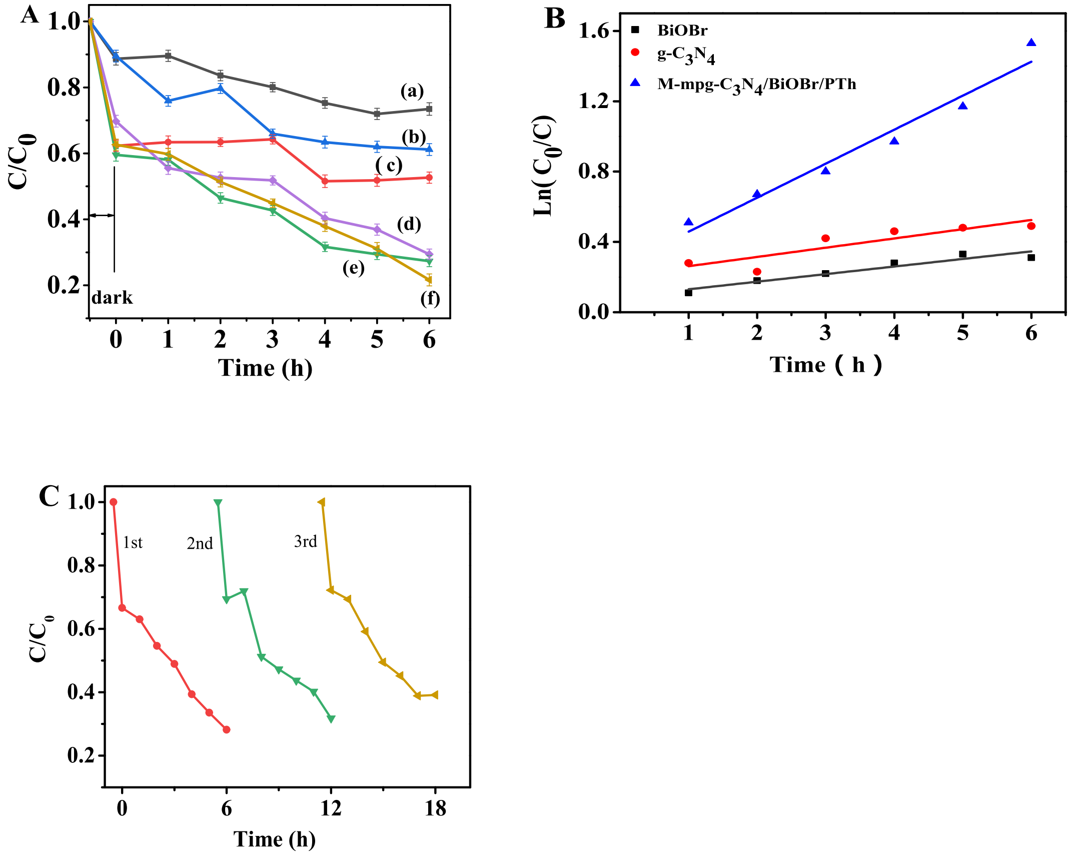

Fig. 9. (A) Photocatalytic degradation of DMP over (a) BiOBr, (b) g-C_3N_4, (c) mpg-C_3N_4, (d) M−mpg−C_3N_4/BiOBr, (e) mpg-C_3N_4/BiOBr/PTh and (f) M−mpg−C_3N_4/BiOBr/PTh under visible light irradiation; (B) The kinetic curves of DMP degradation over different photocatalysts; (C) Cycling times of DMP degradation using M−mpg−C_3N_4/BiOBr/PTh under visible light (photocatalyst:1.0 g/L, DMP: 20 mg/L, pH:7).

mpg-C_3N_4, and BiOBr alone, demonstrating that the photocatalytic performance was enhanced due to the conjunction of mpg-C_3N_4 and BiOBr. Moreover, the photocatalytic DMP degradation efficiency increased after PTh was incorporated into the M−mpg−C_3N_4/BiOBr composite, which coincides with the UV–vis DRS and PL characterization results, indirectly confirming the existence of PTh. The photocatalytic DMP degradation efficiency of M−mpg−C_3N_4/BiOBr/PTh was 40% and 50% higher than that of pristine g-C_3N_4 and BiOBr, respectively. The pseudo first-order kinetic reaction model was used to explore the mechanism of photocatalytic DMP degradation by M−mpg−C_3N_4/BiOBr/PTh, expressed as Eqs. (1) and (2):

$$dC_t/dt = -kC_0 \tag{1}$$

$$-ln(C_t/C_0) = kt \tag{2}$$

where, C_0 and C_t are the DMP concentration at time 0 and t, respectively, mg/L, and k is the pseudo first-order kinetic reaction rate constant, h^{-1}. Using the photocatalytic DMP degradation results, k could be calculated employing equation (2). Fig. 9B indicates that the photocatalytic DMP degradation followed pseudo first-order kinetics, and the reaction rate constants for g-C_3N_4, BiOBr, and M−mpg−C_3N_4/BiOBr/PTh catalysis were 0.052, 0.043, and 0.193 h^{-1}, respectively; thus, that of M−mpg−C_3N_4/BiOBr/

PTh was 3.7- and 4.5-fold higher than that of g-C_3N_4 and BiOBr, respectively. The enhanced photocatalytic performance exhibited by M–mpg–C_3N_4/BiOBr/PTh was principally attributed to the formation of the heterojunction.

The stability and reusability of M–mpg–C_3N_4/BiOBr/PTh was investigated, and the results are shown in Fig. 9C. The photocatalytic DMP degradation efficiency decreased by 3.57% and 10.95% after the second and the third run, respectively, which illustrated that M–mpg–C_3N_4/BiOBr/PTh was stable and reusable for DMP removal from water.

3.3. Effect of pH, dosage, and initial DMP concentration

The effect of pH on the photocatalytic DMP degradation by M–mpg–C_3N_4/BiOBr/PTh was investigated, and the results are displayed in Fig. 10A. DMP could not be detected at pH 11.17 as a result of its decomposition in strong alkaline media. Moreover, the degradation efficiency was the highest under neutral conditions (pH = 7.36). According to a previous report [63], DMP becomes protonated, and thus positively charged, under acidic conditions, as does M–mpg–C_3N_4/BiOBr/PTh; therefore, the electrostatic repulsion between the protons on the photocatalyst surface and the cationic form of DMP possibly leads to deterioration of the photocatalytic efficiency. Analogously, DMP molecules and the photocatalyst surface may become negatively charged under weakly alkaline conditions, likewise reducing the photocatalytic efficiency due to electrostatic repulsion. However, the photocatalytic degradation efficiency was superior under weakly alkaline conditions to that under weakly acidic conditions, which may be attributed to the increased generation of hydroxyl radicals (·OH) from the high amount of OH^- formed under weakly alkaline conditions.

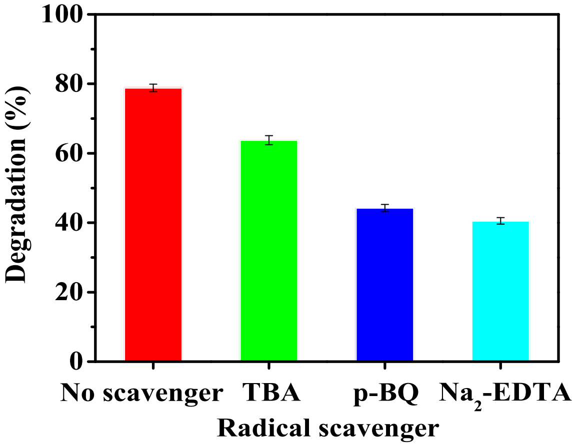

Fig. 11. Effect of different scavengers on photocatalytic degradation of DMP by M–mpg–C_3N_4/BiOBr/PTh (photocatalyst: 1.0 g/L, DMP: 20 mg/L, pH: 7).

The effect of photocatalyst concentration on photocatalytic DMP degradation is illustrated in Fig. 10B. Evidently, exceedingly low or high amounts of photocatalyst were detrimental to photocatalytic DMP degradation. An insufficient dosage could not provide sufficient active sites to generate oxidative radicals, while at very high dosages, the photocatalyst powder increased the turbidity of the solution, limiting light penetration and consequently impeding photocatalyst activation and performance [64].

The effect of initial DMP concentration on the photocatalytic degradation is presented in Fig. 10C. It can be seen that DMP pho-

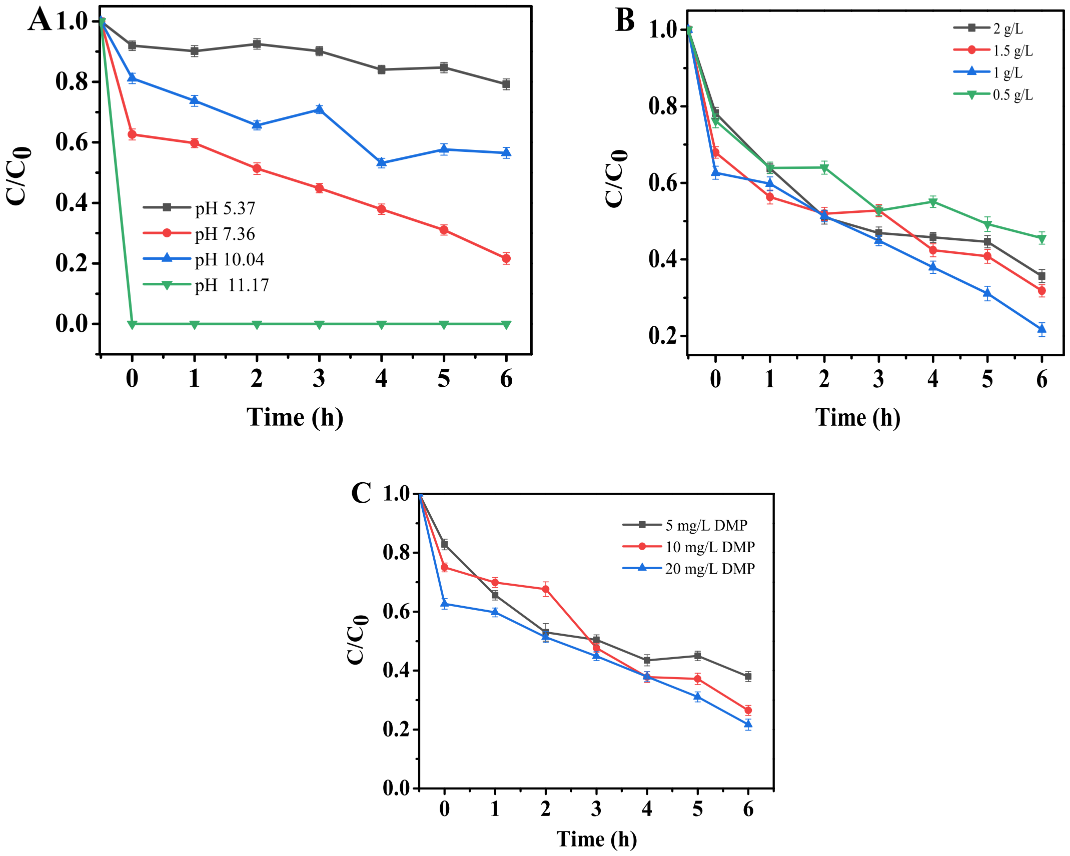

Fig. 10. Photocatalytic degradation of DMP (A) at different pH (photocatalyst: 1.0 g/L, DMP: 20 mg/L), (B) under different dosages of M–mpg–C_3N_4/BiOBr/PTh (DMP: 20 mg/L, pH:7) and (C) different initial concentration of DMP (photocatalyst: 1.0 g/L, pH:7).

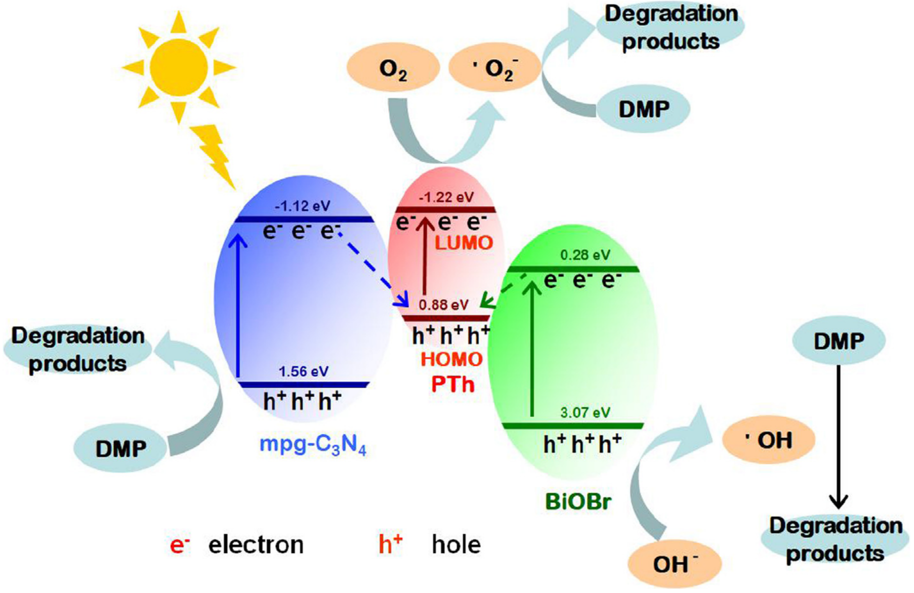

Fig. 12. The schematic of mechanism for DMP photocatalytic degradation over M–mpg–C_3N_4/BiOBr/PTh under visible-light irradiation.

tocatalytic degradation efficiency increased with the increase in initial DMP concentration from 5 to 20 mg/L. A high DMP initial concentration promoted its photocatalytic oxidation, because the driving force of reaction increases with the increase of the number of DMP molecules in high DMP initial concentration.

3.4. Photocatalytic mechanism

In order to elucidate the photocatalytic degradation mechanism, the reactive species were investigated by conducting radical trapping experiments, wherein disodium ethylenediaminetetraacetate (Na_2-EDTA), tertiary butyl alcohol (TBA), and 1,4-benzoquinone (p-BQ) were used as photogenerated hole (h^+), hydroxyl radical ($\cdot OH$), and superoxide radical ($\cdot O_2^-$) scavengers, respectively. The results are demonstrated in Fig. 11. DMP degradation efficiency decreased to 40.54%, 63.58%, and 44.27% with the addition of Na_2-EDTA, TBA, and p-BQ, respectively, indicating the presence of h^+, $\cdot OH$, and $\cdot O_2^-$ active species in the photocatalytic reaction system, and the major role played by h^+ in the degradation of DMP.

Furthermore, to explore the photocatalytic degradation mechanism, the value band (VB) and conduction band (CB) energies of the photocatalysts need to be determined. The VB and CB of mpg-C_3N_4 and BiOBr could be estimated based on Eqs. (3) and (4) as follows [65]:

$$E_{VB} = X - E_e + 1/2E_g \tag{3}$$

$$E_{CB} = E_{VB} - E_g \tag{4}$$

where X is the absolute electronegativity of the semiconductor, E_e is the energy of free electrons on the hydrogen scale (4.5 eV), and E_g is the band gap energy of the photocatalyst. According to Fig. 7B and an Eg of 2.79 eV for BiOBr [66], the E_{VB} and E_{CB} of mpg-C_3N_4 were calculated to be 1.56 and −1.12 eV, respectively, while the E_{VB} and E_{CB} of BiOBr were 3.07 and 0.28 eV, respectively. PTh is a conductive polymer, capable of absorbing photons to excite electrons, which transfer from the ground state of the HOMO to the excited state of the LUMO on account of its π–π^* transition properties under visible light irradiation [57], producing holes and electrons in the HOMO and LUMO, respectively. The band energies of its HOMO and LUMO are 0.88 and −1.22 eV [67], respectively.

A plausible M–mpg–C_3N_4/BiOBr/PTh photocatalytic DMP degradation mechanism is schematically described in Fig. 12. When the heterojunction photocatalyst was irradiated by visible light, mpg-C_3N_4, BiOBr, and PTh were photoexcited to generate electrons and holes. Due to the band structure configuration, a dual Z-scheme electron transfer pathway formed, whereby the photogenerated electrons in the CB of mpg-C_3N_4 and BiOBr tended to migrate to the h + in the HOMO of PTh, and subsequently transfer to the LUMO, the potential of which was more negative than the standard O_2/ $\cdot O_2^-$ redox potential, resulting the O_2 in water capturing electrons to produce $\cdot O_2^-$. Meanwhile, because the h^+ on the VB of BiOBr was more positive than the $\cdot OH/OH^-$ potential, the h^+ could oxidize OH^- (H_2O) to $\cdot OH$. Additionally, the Fe_3O_4 nanoparticles on M–mpg–C_3N_4/BiOBr/PTh acted as an electron transmitter in the process of electron transfer [68]. Thus, the dual Z-scheme electron migration mechanism inhibited the recombination of photogenerated electron-hole pairs in mpg-C_3N_4 and BiOBr, resulting in enhanced photocatalytic activity. Previous EIS measurements (Fig. 8B) supported the inference of effective photogenerated electron-hole pair separation in mpg-C_3N_4 and BiOBr.

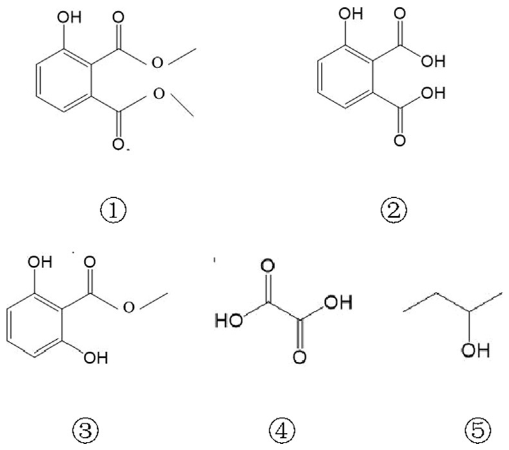

Fig. 13. The intermediate products of photocatalytic DMP degradation.

The intermediate products of the DMP degradation were analyzed using liquid chromatography coupled with mass spectrometry. According to the results, the intermediate products were speculated as shown in Fig. 13. DMP molecules were oxidized to small molecules and finally to CO_2 and H_2O by the h^+, $\cdot O_2^-$, and $\cdot OH$ active species. The mechanism of photocatalytic DMP degradation reaction could be expressed as follows:

$$M-mpg-C_3N_4/BiOBr/PTh + h\upsilon \rightarrow M-mpg-C_3N_4/BiOBr/PTh + (e^-/h^+) \quad (5)$$

$$h^+ + H_2O \rightarrow \cdot OH + H^+ \quad (6)$$

$$e^- + O_2 \rightarrow \cdot O_2^- \quad (7)$$

$$e^- + 0.5O_2 + H_2O \rightarrow \cdot OH + OH^- \quad (8)$$

$$h^+ + OH^- \rightarrow \cdot OH \quad (9)$$

$$h^+ /\cdot OH/ \cdot O_2^- + DMP \rightarrow CO_2 + H_2O + \text{other products} \quad (10)$$

4. Conclusion

A magnetic dual Z-scheme $M-mpg-C_3N_4/BiOBr/PTh$ heterostructure photocatalyst was successfully synthesized via the hydrothermal method, wherein the SSA of $g-C_3N_4$ was increased using SiO_2 templating and acid etching to provide mesoporous $g-C_3N_4$. The formation of the heterostructure effectively enhanced the photocatalytic activity. The photocatalytic DMP degradation efficiency of $M-mpg-C_3N_4/BiOBr/PTh$ was the highest at a photocatalyst dosage of 1.0 g/L in neutral media containing 20 mg/L DMP under visible light; furthermore, it was 40% and 50% higher than that of pristine $g-C_3N_4$ and BiOBr, respectively. The photocatalytic DMP degradation mechanism hinged on the dual Z-scheme electron migration pathway, which inhibited the recombination of photogenerated electron-hole pairs in $mpg-C_3N_4$ and BiOBr. The saturation magnetization of $M-mpg-C_3N_4/BiOBr/PTh$ was 11.31 emu/g. Thus, $M-mpg-C_3N_4/BiOBr/PTh$ could be separated from water in a convenient manner, and reused. The $M-mpg-C_3N_4/BiOBr/PTh$ photocatalyst is an excellent material for the removal of DMP from water.

Declaration of Competing Interest

The authors declare that they have no known competing financial interests or personal relationships that could have appeared to influence the work reported in this paper.

Acknowledgements

This research is supported by the Science and Technology Planning Project of Guangdong Province of China (2013B020800008).

References

[1] S. Li, Z. Chi, W. Li, In vitro toxicity of dimethyl phthalate to human erythrocytes: From the aspects of antioxidant and immune functions, Environ. Pollut. 253 (2019) 239–245.
[2] A.M. Taddesse, T. Bekele, I. Diaz, A. Adgo, Polyaniline supported $CdS/CeO_2/Ag_3PO_4$ nanocomposite: An"A-B"type tandem n-n heterojunctions with enhanced photocatalytic activity, J. Photochem. Photobiol., A: Chem. 406 (2021) 113005.
[3] S.K. Jayaraj, P. Thangadurai, Surface decorated V_2O_5 nanorods with Pt nanoparticles for enriched visible light photocatalytic performance for the photodegradation of Rh-6G, J. Mol. Liq. 319 (2020) 114368.
[4] M. Moradi, Y. Vasseghian, A. Khataee, M. Harati, H. Arfaeinia, Ultrasound-assisted synthesis of $FeTiO_3$/GO nanocomposite for photocatalytic degradation of phenol under visible light irradiation, Sep. Purif. Technol. 261 (2021) 118274.
[5] M. Anjum, R. Kumar, M.A. Barakat, Visible light driven photocatalytic degradation of organic pollutants in wastewater and real sludge using $ZnO–ZnS/Ag_2O–Ag_2S$ nanocomposite, J. Taiwan Institute Chem. Eng. 77 (2017) 227–235.
[6] S. Sultan, Rafiuddin, M.Z. Khan, K. Umar, A.S. Ahmed, M. Shahadat, $SnO_2–SrO$ based nanocomposites and their photocatalytic activity for the treatment of organic pollutants, J. Mol. Struct. 1098 (2015) 393–399.
[7] H. Dong, G. Zeng, L. Tang, C. Fan, C. Zhang, X. He, Y. He, An overview on limitations of TiO_2-based particles for photocatalytic degradation of organic pollutants and the corresponding countermeasures, Water Res. 79 (2015) 128–146.
[8] L. Zheng, X. Xiao, Y. Li, W. Zhang, Enhanced photocatalytic activity of TiO_2 nanoparticles using $WS_2/g-C_3N_4$ hybrid as co-catalyst, Trans. Nonferrous Met. Soc. China 27 (2017) 1117–1126.
[9] Y. Nakai, M. Azuma, M. Muraoka, H. Kobayashi, S. Higashimoto, One-pot imine synthesis from benzylic alcohols and nitrobenzene on CdS-sensitized TiO_2 photocatalysts: Effects of the electric nature of the substituent and solvents on the photocatalytic activity, Mol. Catal. 443 (2017) 203–208.
[10] H. An, Y. Du, T. Wang, C. Wang, W. Hao, J. Zhang, Photocatalytic properties of BiOX (X = Cl, Br, and I), Rare Met. 27 (2008) 243–250.
[11] G. Li, F. Qin, R. Wang, S. Xiao, H. Sun, R. Chen, BiOX (X = Cl, Br, I) nanostructures: Mannitol-mediated microwave synthesis, visible light photocatalytic performance, and Cr(VI) removal capacity, J. Colloid Interface Sci. 409 (2013) 43–51.
[12] X. Zhang, Z. Ai, F. Jia, L. Zhang, Generalized one-pot synthesis, characterization, and photocatalytic activity of hierarchical BiOX (X = Cl, Br, I) nanoplate microspheres, J. Phys. Chem. C 112 (2008) 747–753.
[13] S. Wang, L. Wang, W. Ma, D.M. Johnson, Y. Fang, M. Jia, Y. Huang, Moderate valence band of bismuth oxyhalides (BiOXs, X=Cl, Br, I) for the best photocatalytic degradation efficiency of MC-LR, Chem. Eng. J. 259 (2015) 410–416.
[14] J.C. Ahern, R. Fairchild, J.S. Thomas, J. Carr, H.H. Patterson, Characterization of BiOX compounds as photocatalysts for the degradation of pharmaceuticals in water, Appl. Catal. B: Environ. 179 (2015) 229–238.
[15] J. Li, S. Sun, C. Qian, L. He, K.K. Chen, T. Zhang, Z. Chen, M. Ye, The role of adsorption in photocatalytic degradation of ibuprofen under visible light irradiation by BiOBr microspheres, Chem. Eng. J. 297 (2016) 139–147.
[16] M. Gao, D. Zhang, X. Pu, H. Li, J. Li, X. Shao, K. Ding, BiOBr photocatalysts with tunable exposing proportion of 001 facets: Combustion synthesis, characterization, and high visible-light photocatalytic properties, Mater. Lett. 140 (2015) 31–34.
[17] R. Li, X. Gao, C. Fan, X. Zhang, Y. Wang, Y. Wan, A facile approach for the tunable fabrication of BiOBr photocatalysts with high activity and stability, Appl. Surf. Sci. 355 (2015) 1075–1082.
[18] Y. Wang, Z. Shi, C. Fan, X. Wang, X. Hao, Y. Chi, Synthesis, characterization, and photocatalytic properties of BiOBr catalyst, J. Solid State Chem. 199 (2013) 224–229.
[19] X.X. Zhang, R. Li, M. Jia, S. Wang, Y. Huang, C. Chen, Degradation of ciprofloxacin in aqueous bismuth oxybromide (BiOBr) suspensions under visible light irradiation: A direct hole oxidation pathway, Chem. Eng. J. 274 (2015) 290–297.
[20] Z. Jiang, F. Yang, G. Yang, L. Kong, M.O. Jones, T. Xiao, P.P. Edwards, The hydrothermal synthesis of BiOBr flakes for visible-light-responsive photocatalytic degradation of methyl orange, J. Photochem. Photobiol. A: Chem. 212 (2010) 8–13.
[21] Y. Feng, L. Li, J. Li, J. Wang, L. Liu, Synthesis of mesoporous BiOBr 3D microspheres and their photodecomposition for toluene, J. Hazard. Mater. 192 (2011) 538–544.
[22] J. Xu, W. Meng, Y. Zhang, L. Li, C. Guo, Photocatalytic degradation of tetrabromobisphenol A by mesoporous BiOBr:Efficacy, products and pathway, Appl. Catal. B: Environ. 107 (2011) 355–362.
[23] J. Xu, L. Li, C. Guo, Y. Zhang, S. Wang, Removal of benzotriazole from solution by BiOBr photocatalysis under simulated solar irradiation, Chem. Eng. J. 221 (2013) 230–237.
[24] S. Zarezadeh, A. Habibi-Yangjeh, M. Mousavi, BiOBr and AgBr co-modified ZnO photocatalyst: A novel nanocomposite with p-n-n heterojunctions for highly effective photocatalytic removal of organic contaminants, J. Photochem. Photobiol. A: Chem. 379 (2019) 11–23.
[25] P. Singh, P. Sonu, A. Raizada, P. Sudhaik, P. Shandilya, S. Thakur, V.K. Agarwal, Gupta, Enhanced photocatalytic activity and stability of AgBr/BiOBr/graphene heterojunction for phenol degradation under visible light, J. Saudi Chem. Soc. 23 (2019) 586–599.
[26] S. Zarezadeh, A. Habibi-Yangjeh, M. Mousavi, S. Ghosh, Synthesis of novel p-n-p BiOBr/ZnO/BiOI heterostructures and their efficient photocatalytic performances in removals of dye pollutants under visible ligh, J. Photochem. Photobiol. A: Chem. 389 (2020) 112247.
[27] Q.Y. Tang, M.J. Yang, S.Y. Yang, Y.H. Xu, Enhanced photocatalytic degradation of glyphosate over 2D CoS/BiOBr heterojunctions under visible light irradiation, J. Hazard. Mater. 407 (2021).
[28] H. Liu, B. Wang, M. Chen, H. Zhang, J. Peng, L. Ding, W. Wang, Simple synthesis of BiOAc/BiOBr heterojunction composites for the efficient photocatalytic removal of organic pollutants, Sep. Purif. Technol. 261 (2021) 118286.
[29] X. Yang, Z. Chen, W. Zhao, C. Liu, X. Qian, W. Chang, T. Sun, C. Shen, G. Wei, Construction of porous-hydrangea BiOBr/BiOI n-n heterojunction with enhanced photodegradation of tetracycline hydrochloride under visible light, J. Alloys Compd. 864 (2021) 158–784.

[30] H. Xiao, W. Wang, G. Liu, Z. Chen, K. Lv, J. Zhu, Photocatalytic performances of g-C_3N_4 based catalysts for RhB degradation: Effect of preparation conditions, Appl. Surf. Sci. 358 (2015) 313–318.
[31] H. Ji, F. Chang, X. Hu, W. Qin, J. Shen, Photocatalytic degradation of 2,4,6-trichlorophenol over g-C_3N_4 under visible light irradiatin, Chem. Eng. J. 218 (2013) 183–190.
[32] P. Martín-Ramos, J. Martín-Gil, R.C. Dante, F. Vaquero, R.M. Navarro, J.L.G. Fierro, A simple approach to synthesize g-C_3N_4 with high visible light photoactivity for hydrogen production, Int. J. Hydrogen Energy 40 (2015) 7273–7281.
[33] M. Wu, J.M. Yan, X.W. Zhang, M. Zhao, Synthesis of g-C_3N_4 with heating acetic acid treated melamine and its photocatalytic activity for hydrogen evolution, Appl. Surf. Sci. 354 (2015) 196–200.
[34] L. Ge, Synthesis and photocatalytic performance of novel metal-free g-C_3N_4 photocatalysts, Mater. Lett. 65 (2011) 2652–2654.
[35] J. Liu, Y. Song, H. Xu, X. Zhu, J. Lian, Y. Xu, Y. Zhao, L. Huang, H. Ji, H. Li, Non-metal photocatalyst nitrogen-doped carbon nanotubes modified mpg-C_3N_4: facile synthesis and the enhanced visible-light photocatalytic activity, J. Colloid Interface Sci. 494 (2017) 38–46.
[36] Z. Li, J. Wang, K. Zhu, F. Ma, A. Meng, Ag/ g-C_3N_4 composite nanosheets: Synthesis and enhanced visible photocatalytic activities, Mater. Lett. 145 (2015) 167–170.
[37] J. Singh, P. Kumari, S. Basu, Degradation of toxic industrial dyes using SnO_2/g-C_3N_4 nanocomposites: Role of mass ratio on photocatalytic activity, J. Photochem. Photobiol. A: Chem. 371 (2019) 136–143.
[38] F. Chang, J. Zheng, X. Wang, Q. Xu, B. Deng, X. Hu, X. Liu, Heterojuncted non-metal binary composites silicon carbide/g-C_3N_4 with enhanced photocatalytic performance, Mater. Sci. Semicond. Process. 75 (2018) 183–192.
[39] L. Ge, C. Han, Synthesis of MWNTs/g-C_3N_4 composite photocatalysts with efficient visible light photocatalytic hydrogen evolution activity, Appl. Catal. B: Environ. 117–118 (2012) 268–274.
[40] C. Xing, Z. Wu, D. Jiang, M. Chen, Hydrothermal synthesis of In_2S_3/g-C_3N_4 heterojunctions with enhanced photocatalytic activity, J. Colloid and Interface Sci. 433 (2014) 9–15.
[41] A. Kumar, S. Singh, M. Khanuja, A comparative photocatalytic study of pure and acid-etched template free graphitic C_3N_4 on different dyes: An investigation on the influence of surface modifications, Mater. Chem. Phys. 243 (2020) 122402.
[42] M. Zhang, J. Xu, R. Zong, Y. Zhu, Enhancement of visible light photocatalytic activities via porous structure of g-C_3N_4, Appl. Catal. B: Environ. 147 (2014) 229–235.
[43] G. Tang, F. Zhang, P. Huo, S. Zulfiqarc, J. Xu, Y. Yan, H. Tang, Constructing novel visible-light-driven ternary photocatalyst of AgBr nanoparticles decorated 2D/2D heterojunction of g-C_3N_4/BiOBr nanosheets with remarkably enhanced photocatalytic activity for water-treatment, Ceram. Int. 45 (2019) 19197–19205.
[44] J. Xia, J. Di, S. Yin, H. Li, H. Xu, L. Xu, H. Shu, M. He, Solvothermal synthesis and enhanced visible-light photocatalytic decontamination of bisphenol A (BPA) by g-C_3N_4/BiOBr heterojunctions, Mater. Sci. Semicond. Process. 24 (2014) 96–103.
[45] L. Ye, J. Liu, Z. Jiang, T. Peng, L. Zan, Facets coupling of BiOBr-g-C_3N_4 composite photocatalyst for enhanced visible-light-driven photocatalytic activity, Appl. Catal. B: Environ. 142–143 (2013) 1–7.
[46] J. Lv, K. Dai, J. Zhan, Q. Liu, C. Liang, G. Zhu, Facile constructing novel 2D porous g-C_3N_4/BiOBr hybrid with enhanced visible-light-driven photocatalytic activity, Sep. Purif. Technol. 178 (2017) 6–17.
[47] Z. Shi, Y. Zhang, X. Shen, G. Duoerkun, B. Zhu, L. Zhang, M. Li, Z. Chen, Fabrication of g-C_3N_4/BiOBr heterojunctions on carbon fibers as weaveable photocatalyst for degrading tetracycline hydrochloride under visible light, Chem. Eng. J. 386 (2020) 124010.
[48] L. Yang, L. Liang, L. Wang, J. Zhu, S. Gao, X. Xia, Accelerated photocatalytic oxidation of carbamazepine by a novel 3D hierarchical protonated g-C_3N_4/BiOBr heterojunction: Performance and mechanism, Appl. Surf. Sci. 473 (2019) 527–539.
[49] X. Zhou, B. Jin, R. Chen, F. Peng, Y. Fang, Synthesis of porous Fe_3O_4/g-C_3N_4 nanospheres as highly efficient and recyclable photocatalysts, Mater. Res. Bull. 48 (2013) 1447–1452.
[50] M. Mousavi, A. Habibi-Yangjeh, D. Seifzadeh, Novel ternary g-C_3N_4/Fe_3O_4/$MnWO_4$ nanocomposites: Synthesis, characterization, and visible-light photocatalytic performance for environmental purposes, J. Mater. Sci. Technol. 34 (2018) 1638–1651.
[51] C. Ai, S.C. Wu, L.Y. Li, Y. Lei, X. Shao, Novel magnetically separable γ-Fe_2O_3/Ag/AgCl/g-C_3N_4 composite for enhanced disinfection under visible light, Colloids Surf. A 583 (2019) 123981.
[52] E.M. Khudhair, S.H. Ammar, H.J. Khadim, Phosphotungstic acid immobilized onto ZnO coated zerovalent iron (Fe@ZnO/PW) core/shell magnetic nanocomposite for enhanced photocatalytic bacterial inactivation under visible light, J. Photochem. Photobiol. A: Chem. 404 (2021) 112907.
[53] J. Singh, S. Basu, Synthesis of mesoporous magnetic Fe_2O_3/g-C_3N_4 monoliths for Rhodamine B removal, Microporous Mesoporous Mater. 303 (2020) 110299.
[54] K. Dutta, D. Rana, Polythiophenes: An emerging class of promising water purifying materials, Eur. Polym. J. 116 (2019) 370–385.
[55] S. Li, M. He, Z. Li, D. Li, Z. Pan, Removal of humic acid from aqueous solution by magnetic multi-walled carbon nanotubes decorated with calcium, J. Mol. Liq. 230 (2017) 520–528.
[56] M.R. Mahmoudian, W.J. Basirun, Y. Alias, M.W. Pei, Investigating the effectiveness of g-C_3N_4 on Pt/g-C_3N_4/polythiophene nanocomposites performance as an electrochemical sensor for Hg^{2+} detection, J. Environ. Chem. Eng. 8 (2020) 104204.
[57] L. Wang, H. Zhang, C. Guo, L. Feng, C. Li, W. Wang, Facile constructing plasmonic Z-scheme Au NPs/ g-C_3N_4/BiOBr for enhanced visible light photocatalytic activity, J. Fuel Chem. Technol. 47 (2019) 834–842.
[58] M. Faisal, F.A. Harraz, M. Jalalah, M. Alsaiari, S.A. Al-Sayari, M.S. Al-Assiri, Polythiophene doped ZnO nanostructures synthesized by modified sol-gel and oxidative polymerization for efficient photodegradation of methylene blue and gemifloxacin antibiotic, Mater. Today Commun. 24 (2020) 101048.
[59] M.R. Gholipour, F. Béland, T.O. Do, Post-calcined carbon nitride nanosheets as an efficient photocatalyst for hydrogen production under visible light irradiation, ACS Sustainable Chem. Eng. 5 (2016) 213–220.
[60] N. Liu, J. Wang, J. Wu, Z. Li, W. Huang, Y. Zheng, J. Lei, X. Zhang, L. Tang, Magnetic Fe_3O_4@MIL-53(Fe) nanocomposites derived from MIL-53(Fe) for the photocatalytic degradation of ibuprofen under visible light irradiation, Mater. Res. Bull. 132 (2020) 111000.
[61] N. Liu, Y. Zheng, C. Jing, B. Gao, W. Huang, Z. Li, J. Lei, X. Zhang, L. Cui, L. Tang, Boosting catalytic degradation efficiency by incorporation of MIL-53(Fe) with Ti3C2Tx nanosheeets, J. Mol. Liq. 311 (2020) 113201.
[62] H. Jing, R. Ou, H. Yu, Y. Zhao, Y. Lu, M. Huo, H. Huo, X. Wang, Engineering of g-C_3N_4 nanoparticles/WO_3 hollow microspheres photocatalyst with Z-scheme heterostructure for boosting tetracycline hydrochloride degradation, Sep. Purif. Technol. 255 (2021) 117646.
[63] S. Akbari, G. Moussavi, S. Giannakis, Efficient photocatalytic degradation of ciprofloxacin under UVA-LED, using S, N-doped MgO nanoparticles: Synthesis, parametrization and mechanistic, J. Mol. Liq. 324 (2021) 114831.
[64] M. Aram, M. Farhadian, A.R. Solaimany Nazar, S. Tangestaninejad, P. Eskandari, B.-H. Jeon, Metronidazole and Cephalexin degradation by using of Urea/TiO_2/$ZnFe_2O_4$/Clinoptiloite catalyst under visible-light irradiation and ozone injection, J. Mol. Liq. 304 (2020) 112764.
[65] Z. Geng, Y. Zhang, X. Yuan, M. Huo, Y. Zhao, Y. Lu, Y. Qiu, Incorporation of Cu_2O nanocrystals into TiO_2 photonic crystal for enhanced UV-visible light d- riven photocatalysis, J. Alloys Comp. 644 (2015) 734–741.
[66] Z. Yang, J. Li, F. Cheng, X. Dong, BiOBr/protonated graphitic C_3N_4 heterojunctions: Intimate interfaces by electrostatic interaction and enhanced photocatalytic activity[J], J. Alloys Compd. 634 (2015) 215–222.
[67] T. Zhou, The controllable construction of BiOBr composites and their photocatalytic applications, Jiangsu University, Zhengjiang, 2018, https://kns.cnki.net.
[68] J. Li, F. Yang, Q. Zhou, R. Ren, L. Wu, Y. Lv, A regularly combined magnetic 3D hierarchical Fe_3O_4/BiOBr heterostructure: Fabrication, visible-light photocatalytic activity and degradation mechanism, J. Colloid Interface Sci. 546 (2019) 139–151.